Earthquake nucleation characteristics revealed by seismicity response to seasonal stress variations induced by gas production at Groningen.

Mateo Acosta[1*], Jean-Philippe Avouac[1,2], Jonathan D. Smith[1], Krittanon Sirorattanakul[1], Hojjat Kaveh[1,2], Stephen J. Bourne[3]

[1]Division of Geological and Planetary Sciences (GPS), California Institute of Technology, Pasadena, CA, USA.

[2]Mechanical and Civil Engineering (MCE), California Institute of Technology, Pasadena, CA, USA.

[3]Shell Global Solutions, Amsterdam, NL.

*Corresponding author. Mateo Acosta: acosta@caltech.edu

Key Points:

- An improved reservoir, geomechanical, and seismicity modelling workflow is proposed for forecasting induced seismicity at various timescales.
- Short-timescale stress variations allow constraining the characteristics of the earthquake nucleation process using Groningen as case study.
- Initial strength excess and finite duration of the nucleation process allow reproducing long-and-short timescale characteristics of seismicity.

Abstract

Deterministic earthquake prediction remains elusive, but time-dependent probabilistic seismicity forecasting seems within reach thanks to the development of physics-based models relating seismicity to stress changes. Difficulties include constraining the earthquake nucleation model and fault initial stress state. Here, we analyze induced earthquakes from the Groningen gas field, where production is strongly seasonal, and seismicity began 3 decades after production started. We use the seismicity response to stress variations to constrain the earthquake nucleation process and calibrate models for time-dependent forecasting of induced earthquakes. Remarkable agreements of modelled and observed seismicity are obtained when we consider (i) the initial strength excess, (ii) the finite duration of earthquake nucleation, and (iii) the seasonal variations of gas production. We propose a novel metric to quantify the nucleation model's ability to capture the damped amplitude and the phase of the seismicity response to short-timescale (seasonal) stress variations which allows further tightening the model's parameters.

Plain Language Summary

Earthquakes are difficult to predict with certainty, but progress in forecasting their likelihood using probabilistic models based on stress changes has been made. However, challenges remain in understanding how earthquakes start and the initial conditions of faults. Here, we analyzed induced earthquakes in the Groningen gas field, where production is seasonal and seismic activity began 34 years after gas production started. By studying how the earthquakes respond to rapid changes in stress, we could better understand how they start and develop models to forecast their temporal occurrence. By considering factors like the initial strength of the faults, the duration of earthquake initiation, and seasonal variations in gas production we could accurately match the observed seismic activity. We introduced a new measure to evaluate how well the models captured the dampened strength and timing of seismic activity in response to short-term stress changes (such as seasonal variations), which helped refine the model's parameters.

1 Introduction

Numerous activities related to the decarbonization, or security of energy production involve managing subsurface reservoirs (geothermal, CO_2 sequestration, hydrogen storage, conventional and unconventional oil-and-gas extraction). Induced earthquakes are a major obstacle to these activities (Candela, et al., 2018; Ellsworth, 2013; Goebel & Brodsky, 2018; Grigoli, et al., 2017; Kaven, et al., 2015; Raleigh, et al., 1976; Shirzaei, et al., 2016; Walsh & Zoback, 2015; Zhai, et al., 2019) raising the need for improved methods to forecast induced seismicity. The modern understanding that earthquakes result from unstable frictional fault slip (Scholz, 2019) provides a foundation to forecast changes of earthquake rate in response to stress changes, ΔS (Bourne, et al., 2018; Bourne & Oates, 2017; Dahm & Hainzl, 2022; Dempsey & Suckale, 2017; Dempsey & Suckale, 2023; King, et al., 1994; Kühn, et al., 2022; Langenbruch, et al., 2018; Richter, et al., 2020; Zhai, et al., 2019). The approach requires a model of earthquake nucleation and knowledge of the stress change needed to initiate it (strength excess). At its simplest, the standard Coulomb friction model, CF, assumes that unstable fault slip initiates instantaneously when the ratio of shear stress to effective normal stress exceeds the static friction coefficient. In this context, the often-observed lagged response of the seismicity to stress changes can be modeled through an initial strength excess (Bourne & Oates, 2017). While the CF approach has been found satisfying in several case studies (Bourne, et al., 2018; Bourne

& Oates, 2017; Dempsey & Suckale, 2017; Dempsey & Suckale, 2023; Smith, et al., 2022), this model neglects that earthquake nucleation might not be instantaneous, as evidenced by laboratory experiments (Dieterich, 1994) and the weak correlation of earthquakes with solid Earth tides (Beeler & Lockner, 2003; Cochran, et al., 2004). Some models have introduced an *ad-hoc* critical time-to-failure (Dahm & Hainzl, 2022; Zhai, et al., 2019) to account for either the initial strength excess or non-instantaneous nucleation. A more physical way to account for the finite duration of the nucleation process consists in assuming that nucleation is governed by rate-and-state friction, RS, (Dieterich, 1994), a model adopted with success in a number of studies (Candela, et al., 2019; Candela, et al., 2022; Langenbruch, et al., 2018; Richter, et al., 2020). Discriminating between the CF and RS models has however proven elusive (Dempsey & Suckale, 2023) due to the lack of observational constraints on the nucleation process, and the eventual trade-off between the initial strength excess and the nucleation time. The CF and RS models yield very different forecasts if stress changes occur at short timescales compared to the characteristic time of the nucleation process (Heimisson, et al., 2022), and the nucleation process might therefore be revealed from the seismicity response to large amplitude, short-timescale stress variations (Ader, et al., 2014). Here we demonstrate that the nucleation process is not instantaneous and derive constraints on its characteristic timescales, fault friction parameters, and the initial strength excess by studying seismicity induced by gas extraction from the Groningen field, where strong seasonal variations of gas production (Figure 1A,B) generated significant seasonal seismicity variations.

The Groningen gas field in northeastern Netherlands (Figure 1A) is an ideal example to study induced seismicity due to well-known reservoir properties (Burkitov et al., 2016; de Jager & Visser, 2017; Oates, et al., 2022), detailed seismicity catalog (Dost, et al., 2017; Smith, et al., 2020; Willacy, et al., 2018), and well-resolved surface subsidence (Smith, et al., 2019; van Thienen-Visser & Breunese, 2015). Together, these data have allowed for calibration of models used to hindcast and forecast induced seismicity (Bourne, et al., 2014; Bourne, et al., 2018; Bourne & Oates, 2017; Buijze, et al., 2017; Candela, et al., 2019; Candela, et al., 2022; Dahm & Hainzl, 2022; Dempsey & Suckale, 2017; Dempsey & Suckale, 2023; Heimisson, et al., 2022) (Kühn, et al., 2022; Meyer, et al., 2022; Richter, et al., 2020; Van Wees, et al., 2017). Gas is extracted from a thin, laterally extensive (~100-300 m thickness for ~30*50 km horizontal dimension), porous and permeable (~15-20% porosity, ~3.55E-13 m^2 permeability (de Jager & Visser, 2017; Meyer et al., 2022)) reservoir hosted in the Rotliegend sandstone formation (Figure 1A,B). Production started in 1963 but earthquakes were not detected until 1991. Initially, the seismicity rate increased exponentially, despite annual extraction rates not being at their peak (Figure 1B, green curve). The 2012 M_w3.6 Huizinge earthquake, the largest event to date, caused public concern and a decision to decrease first and then shut-down production long before exhaustion of the gas reserve (de Waal, et al., 2015; Muntendam-Bos, et al., 2017; van Thienen-Visser & Breunese, 2015). The reduction in production was accompanied with a reduction of the seasonal variations of extraction as these variations were thought to increase the total seismicity (Muntendam-Bos & De Waal, 2013; Sijacic, et al., 2017). More details about the gas field and the available data are given in Supplementary Item 1.

The various stress-based models developed so far consider either instantaneous seismicity nucleation with an initial strength excess (Bourne, et al., 2018; Bourne & Oates, 2017; Dempsey & Suckale, 2017; Dempsey & Suckale, 2023; Meyer, et al., 2022; Smith, et al., 2022) a delayed response due to the nucleation process (Candela, et al., 2019; Candela, et al., 2022; Kühn, et al., 2022; Dahm & Hainzl, 2022; Richter, et al., 2020) or a combination of both (Dahm & Hainzl, 2022; Heimisson, et al., 2022). These models fit well the observed seismicity based on yearly averaged stress changes, but predict drastically different responses to rapid variations of production such as shut-ins (Heimisson, et al., 2022; Meyer, et al., 2022). Moreover, a bias could be introduced as these models were calibrated ignoring that, in reality, gas extractions show ~60-80% larger production in the winter from 1975 to 2013 (Figure 1B). Ignoring short-timescale, large-amplitude stress variations could bias the model because the seismicity response to stress changes is non-linear: the CF is non-linear through the initial strength excess and Kaiser effect (seismicity rate drops to zero when the Coulomb stress is lower than previous peak values); the RS includes a delayed Kaiser effect and, adding further non-linearity, an exponential dependence on ΔS (Heimisson & Segall, 2018). The introduction of a stress threshold, if an initial strength excess is allowed, is another source of non-linearity (Heimisson et al., 2022). Hereafter, we compare models with or without accounting for seasonal stress variations to illuminate the characteristics of the nucleation process.

2 Materials and Methods

We present a summary of the modelling strategy (Figure S1) that allows us to resolve (i) the pore pressure diffusion due to injection/extraction from a porous reservoir, (ii) the mechanical response of the reservoir to pressure variations, and (iii) the relation between stress changes and seismicity adopted in this study. We then present the fundamentals of other analysis techniques used such as the synthetic catalog generation, the Schuster test, and the metric to quantify seasonality in synthetic catalogs.

2.1 Modelling workflow

Our modeling workflow (Figure S1) consists of different modules which allow us to predict reservoir pressure, stress changes within and outside the reservoir, subsidence and seismicity based on the gas extraction flow rates at the wells. The parameters for the different modules are optimized from matching the observations (well pressure, subsidence, seismicity).

2.1.1 From fluid extraction to pressure changes.

To relate fluid extraction to pressure changes in the reservoir, we use a simplified reservoir model (Meyer, et al., 2022) which assumes vertical flow equilibrium (VFE) to compute fluid pressure diffusion in the reservoir from the extraction history. This model assumes that the timescale for vertical pressure equilibrium is much shorter than the horizontal one due to the thin and elongated geometry of the reservoir. The problem becomes a two-dimensional one and we solve the combined conservation of momentum and Darcy's law using the open-source finite element library FEniCS (Logg, et al., 2012) and calibrate the model's parameters by history matching the well pressure time-histories. By reducing the computation cost using the VFE assumption, we can generate pressure ($\Delta p(x, y, t)$) space-time histories in the Groningen reservoir with 1-month temporal discretization, allowing us for the first time to quantify the effect of seasonal variations of extraction in the pressure field (See Supplementary Item 2.1 for details).

2.1.2 From pressure changes to reservoir deformation and stress changes.

We use the poroelastic mechanical model from (Smith, et al., 2022) to relate the fluid pressure changes to stress changes within and outside the reservoir.

$\Delta p(x, y, t)$ calculated using the VFE reservoir model (section 2.2.1) is combined with the geodetically derived uniaxial compressibility ($C_m(x, y)$; (Smith, et al., 2019)), and the reservoir thickness ($h(x, y)$) such that the reservoir compaction writes:

$$C = C_m(x, y).\Delta p(x, y, t).h(x, y) \quad (1)$$

We use a semi analytical Green's function approach (Geertsma, 1973; Kuvshinov, 2008) to relate compaction and displacement/stress. For details on the functions, the spatial smoothing used and the details on the stress calculation, see (Smith, et al., 2022); and Supplementary Item 2.2. From the changes in shear stress, $\Delta\tau$, and effective normal stress ($\Delta\sigma'_N = \Delta\sigma_N - \Delta p$), we compute the changes in Coulomb stress, $\Delta S(x, y, t)$, computed 10 m above the reservoir and cumulated since 1960 (Figure 2A). We use a positive sign for compressive stress such that

$\Delta S = \Delta\tau + f.\Delta\sigma'_N$, with f the static friction coefficient of the rock. In this field, the fault's dips are usually ~85º and the strikes show two dominant modes at N270◦ E and N350◦ E ((Smith, et al., 2022); Figure 1A). We use the maximum Coulomb stress changes for both dominant receiver fault strike modes but results show little sensitivity to this choice (Smith, et al., 2022), the chosen depth for calculation, and to f. Our model is computationally efficient and consistent with the 3-D stress changes computed using other methods (Bourne, et al., 2018; Bourne & Oates, 2017; Buijze, et al., 2017; Candela, et al., 2019; Candela, et al., 2022; Kühn, et al., 2022; Van Wees, et al., 2017). For detailed analysis of the effect of the different parameters of the model on seismicity forecasts, see (Smith, et al., 2022). Under reasonable stress sampling schemes, the forecasts are little affected by the choice of the stress model. Changing the stress model has the effect of rescaling the inverted seismicity model parameters but does not drastically affect the seismicity forecasts (Kaveh, et al., 2023).

2.2.3 From stress changes to seismicity rate changes

Finally, we relate ΔS to the time-dependent seismicity rate change ΔR using the Threshold Rate and State failure function (TRS) of (Heimisson, et al., 2022) which follows Dieterich's hypothesis (Dieterich, 1994) that earthquake nucleation is governed by rate and state friction but allows for a population of faults to be sub-critical initially (below steady-state), as expected in a quiet, intraplate tectonic context such as Groningen. A critical stress threshold (analog to the strength excess of the Coulomb Failure model) ΔS_c has to be overcome to reach self-sustained fault slip acceleration (earthquake nucleation) and produce seismicity (Heimisson, et al., 2022). The TRS model writes for every point in space (x, y):

$$\frac{\Delta R(t)}{r} = \frac{\exp\left(\frac{\Delta S(t) - \Delta S_c}{A\sigma_0}\right)}{\frac{1}{t_a}\int_{t_b}^{t} \exp\left(\frac{\Delta S(t') - \Delta S_c}{A\sigma_0}\right) dt' + 1}$$

if $t \geq t_b$, and (2)

$$\frac{\Delta R}{r} = 0$$

if $t \leq t_b$,

with r the background seismicity rate (the seismicity rate that results from constant tectonic loading), $\Delta S(t)$ the change in Coulomb stress, ΔS_c the critical stress threshold, $A\sigma_0$ the frictional-stress parameter of Rate and State friction (Dieterich, 1994), t_a the characteristic time associated to the nucleation process characterizing the decay of seismicity to background rates after a stress step. Finally, t_b is the time at which ΔS first exceeded ΔS_c.

When the sources are critically stressed, $\Delta S_c \sim 0$, the formulation (Eq.2) is equivalent to that of (Heimisson & Segall, 2018). The characteristic time, t_a relates to the secular background stressing rate, due to tectonic loading, $\dot{\tau}$ according to $t_a = \frac{A\sigma_0}{\dot{\tau}}$. It characterizes the nucleation process under such loading and would characterize the response time of the seismicity to a stress step added to the background seismicity. Note that if the system has been stressed, the relaxation time will change as described in section 3.2. The TRS formulation allows for earthquake nucleation to be time dependent and nucleation would be nearly instantaneous in the limit where its response time goes to zero, as is assumed in the standard Coulomb failure model which is also commonly used to relate stress changes to seismicity (Dempsey & Suckale, 2017; Bourne & Oates, 2017; Bourne, et al., 2018; Dempsey & Suckale, 2023; Meyer, et al., 2022; Smith, et al., 2022).

We sample a probability distribution of the TRS model parameters using an ensemble Markov Chain Monte Carlo ($MCMC$) algorithm (Foreman-Mackey, et al., 2013) implemented in PyMC3 (Salvatier, et al., 2016) with uniform priors and a non-local Poisson log-likelihood function (See supplementary Item 2.3). For all TRS models generated in this study, we discretize the stress changes on a monthly basis to avoid numerical integration problems when comparing monthly and yearly discretizations. The difference between the 'monthly' and 'yearly' TRS model inversions presented hereafter is that the input stress changes and seismicity for the 'yearly' models are smoothened using a 12-month average for the whole time-history. The posterior parameter space accounts therefore for epistemic uncertainty on the model's parameters. We report the 1000 model parameter sets with the lowest negative log-likelihood calculated over the training period only. This allows us to compare constraints on TRS models accounting or not for seasonal variations. Equivalently, if we were to consider goodness of fit from given confidence bounds, the number of models falling within a fixed interval would bring information about the constraints on the TRS model parameters.

Then, from the inverted model parameters we can generate the seismicity rates for the whole reservoir as function of time, $R(t)$. Finally, to generate earthquake catalogs we need to account for the aleatoric variability around the predicted rates which accounts for the fact that the earthquake generation is a non-stationary Poisson process of known rate. Details on the synthetic catalog generation are given in Supplementary Item 3.

2.2 Testing seasonality through the Schuster test & spectrum.

We test possible seasonality (periodicities) in the observed and synthetic seismicity catalogs using the Schuster test (Ader & Avouac, 2013; Beeler & Lockner, 2003; Schuster, 1897). For a tested period T, a phase θ_i is associated to each event i occurring at time t_i such that $\theta_i = 2\pi \frac{t_i}{T}$. Then, a 2D walk of N successive unit length steps in the phase direction are performed. The total distance D between the start and end points of the walk relates to the Schuster *p-value* which measures the probability that the walked length is the result of a random Poisson point process as $p = e^{-\frac{D^2}{N}}$, with N the total number of steps taken. Thus, the lower this *p-value*, the higher the probability that the detected periodicity is real. To study the correlation with a periodic perturbation, we evaluate the *p-value* over a continuous range of periods $T \in [T_0, T_1]$ e.g. we evaluate the Schuster spectrum (Ader & Avouac, 2013). The measured *p-values* can then be compared with the expected value, which depends on the tested period, not to be exceeded at a certain confidence level. The spectrum allows for identification of periodicities that have little probability to be due to chance because periodicities in the earthquake catalog will show as isolated low *p-values* in the spectrum, and event clusters will show as a drifting low *p-value* close to the characteristic time of the cluster (Ader & Avouac, 2013).

We define a new metric to characterize the capacity of the TRS models to capture seasonality as the vector distance error of the median of all synthetic catalog's Schuster random walks to that of the observed catalog. To separate their contribution, we also compute the phase, and distance errors for the median of all synthetic catalogs to the observed catalog. See Supplementary Item 4 for details. This analysis allows to quantify the model's capacity of reproducing the amplitude and phase of the seasonal variations in the observed earthquake catalog.

3 Results and discussion

3.1 TRS model parameters not accounting for seasonal stress changes: 'yearly' models.

When seasonal fluctuations of ΔS and seismicity are ignored (Figure 1D, light purple curve), we obtain a 'yearly' TRS model which fits well the temporal (Figure 2A, green curve) and spatial distributions (Figure 2C) of seismicity. The prediction of the maximum-a-posteriori (MAP) yearly TRS model at the annual time scale is satisfying. However, if a range of acceptable models is considered (1000 best models out of 50,000, accounting for epistemic uncertainty, see (Kaveh, et al., 2023) for details), they yield widely different predictions outside the training period due to large trade-offs among the model parameters, especially between t_a and r (Figure S3). The response time of seismicity to sub-annual stress variations is not well constrained in this inversion. To illustrate this effect, the green curves in Figure 2B show the response of the 1000 best yearly TRS models assuming no stress-changes after 2012 (frozen to $\Delta S(t_s)$, mimicking a hypothetical 'shut-in' at time t_s). The relaxation following the 'shut-in' is not characterized by t_a, (10-10,000 years for yearly TRS models), but by a new "accelerated" response time t_{acc} such that equation (2) becomes:

$$\frac{\Delta R}{r} = \frac{\exp\left(\frac{\Delta S(t_s)-\Delta S_c}{A\sigma_0}\right)}{1+\frac{1}{t_a}\int_{t_b}^{t_s}\exp\left(\frac{\Delta S(t')-\Delta S_c}{A\sigma_0}\right)dt' + (t-t_s)\left(\frac{\exp\left(\frac{\Delta S(t_s)-\Delta S_c}{A\sigma_0}\right)}{t_a}\right)}$$

$$\frac{\Delta R}{r} = \frac{t_a}{(t-t_s)+\frac{t_a+\int_{t_b}^{t_s}\exp\left(\frac{\Delta S(t')-\Delta S_c}{A\sigma_0}\right)dt'}{\exp\left(\frac{\Delta S(t_s)-\Delta S_c}{A\sigma_0}\right)}} \tag{3}$$

We can identify this to the form:

$$\frac{\Delta R(t)}{r} = \frac{t_a}{(t-t_s)+t^{acc}}$$

whose characteristic decay time is:

$$t_a^{acc} = \frac{\left(t_a+\int_{t_b}^{t_s}\exp\left(\frac{\Delta S(t')-\Delta S_c}{A\sigma_0}\right)dt'\right)}{\exp\left(\frac{\Delta S(t_s)-\Delta S_c}{A\sigma_0}\right)} \tag{4}$$

t_a^{acc} becomes much shorter than t_a because the nucleation process is accelerated exponentially due to stress increase induced by the reservoir compaction. Assuming an approximately linear increase of $\Delta S(t)$ at the multiannual time scale, it converges quickly toward $t_a^{acc}(t_s) \sim \frac{A\sigma_0 . \Delta t}{\Delta S(t_s)}$ where Δt is the duration of production from onset of seismicity to "shut in". It is therefore inversely proportional to the average stressing rate: $\frac{\Delta S(t_s)}{\Delta t}$, and proportional to $A\sigma_0$. In effect, our best yearly TRS models show t_a^{acc} ranging from 0.1 to 200 years after a hypothetical shut-in, showing that $A\sigma_0$ is poorly constrained (Figure S4, green curves, Figure S3A).

3.2 Seasonal stress changes effect on model parameter inversion: 'monthly' models.

We next take seasonal stress variations into account (Figure 3, Figure 1B,D). At the sub-yearly timescale, pressure is not homogenized over the whole reservoir. Given the permeability (k~3.55e-13 m^2) and porosity (ϕ~15%) of the reservoir, its average hydraulic diffusivity is α_{hy}~0.5 m^2/s and its characteristic diffusion length over one year is $r_{hy} = \sqrt{2\pi\alpha_{hy}t}$ ~10 km which is smaller than the minimum length scale from any well cluster to the reservoir's edge (Figure 1B), effectively resulting in smeared seasonal reservoir pressure. This damping effect and the heterogeneity in reservoir compressibility (Burkitov et al., 2016; Smith, et al., 2019) control the spatial distribution of seasonal ΔS amplitude (Figure 3D) which can reach ~20 kPa (Figure 3A, B). The effect of seasonal stress variations could be significant if the seismicity response to stress changes is fast enough. Figure 3E compares the observed seasonal variation of seismicity rate, obtained by stacking monthly earthquakes for all years (orange curve), with the stack of rates expected for the CF model with instantaneous nucleation (Figure 3E, yellow curve). In that case, since the stress evolution is monotonic, the seismicity rate is proportional to the Coulomb stress rate, $\Delta\dot{S}$ (Ader & Avouac, 2013; Dempsey & Suckale, 2017). The observed seasonal variation is much smaller than predicted by the instantaneous nucleation model and is out of phase by about 3 months. A time dependent nucleation process can in principle explain both the phase shift and the damped response (Ader & Avouac, 2013) as explored next.

We construct a 'monthly' TRS model which accounts for seasonal stress variations. The stress changes are computed using monthly gas extractions accounting for seasonality (Figure 3, Figure 1D, blue curve). The 'monthly' and 'yearly' TRS models predict temporal (Figure 2A) and spatial (Figure 2C,D) distributions of seismicity that fit equally well the observations (Figure 2E) but yield significantly different posterior model parameter distributions (Figure S3). When seasonality in ΔS is accounted for, both the product $r.t_a$ and $A\sigma_0$ are tightly constrained (Figure S3, blue points). The available seismic catalog is insufficient to derive good constraints on the background seismicity rate so the trade-off between t_a and r cannot be resolved, but the performance of the forecast is good as it depends chiefly on $r.t_a$ and $A\sigma_0$ which are relatively well constrained. Better constraints in the 'monthly' TRS model parameters lead to consistently shorter and more tightly constrained relaxation times in response to changes in ΔS (Figure 2B, Figure S4). The annual stack of seismicity shows that the "yearly" models (Figure3E, green curves) predict no seasonality with an average of ~35 to 90 events/month, confirming indeed large epistemic uncertainty. On the other hand, the "monthly" models (Figure 3E, blue curves) show a consistent stack with the observed catalog and a drastically reduced epistemic uncertainty as explored below.

3.3 Constraining the nucleation characteristics from earthquake seasonality.

We now assess the ability of the TRS models to explain both the phase and amplitude of the seismicity response to seasonal stress variations. We adopt the Schuster test & spectrum ((Ader

& Avouac, 2013), Supplementary Item 3) which allows searching for any possible periodicity by building a spectrum of the Schuster *p-values*. The Schuster spectrum calculated on the 1991-2022 Groningen earthquake catalog (Dost, et al., 2017; KNMI, 2023) for $M \geq 1.1$, shows a significant, isolated periodicity at 1-year period (Figure 4, orange colors, Figure S6). The Schuster *p-value* at 1 year (~2.4e-3) uniquely falls above 90% confidence level (meaning the chance of one tested period yielding such a low *p-value* being due to chance is less than 10%). The corresponding Schuster walk at 1-year (Figure 4, orange wiggles, (Beeler & Lockner, 2003; Noël, et al., 2019)) shows consistent year to year drift indicative of excess seismicity in the winter, peaking between March and April, delayed with respect to peak extraction rates in January but synchronized with the maximum amplitude of calculated pressure, and ΔS in most of the reservoir (Figure 3D, and orange tick in Figure 4C,D). Note that if smaller earthquakes were considered in the analysis, the seasonality amplitude would become larger (Figure S6). The Schuster test and spectrum are not affected by the use of different magnitudes of completion, but we keep only events with magnitude ≥ 1.1 for consistency with the presented earthquake forecasts. To test if the observed seasonality is predicted by TRS models, we generate 100 synthetic catalogs from the MAP TRS models accounting for aleatoric variability in the seismicity generation (Figure S5) and calculate a Schuster spectrum (Figure 4A,B) and a Schuster walk at 1 year period (Figure 4C, D) for each catalog. The catalogs generated with the monthly TRS model (accounting for seasonal stress variations in the model inference and forecast) show clear periodicity at 1-year period with p-values centered around the observed catalog ones, quantitatively recovering the amplitude of seasonality (Figure 4A, blue dots). Remarkably, the synthetic catalogs generated from the MAP 'monthly' TRS model (Figure 4C, blue wiggles) show a marked drift, with similar phase and amplitude as the observed catalog. We also generate synthetic catalogs using the MAP parameters of the 'yearly' TRS model but using the seasonal variation of ΔS in input (Figure 4B, D, green colors). These example catalogs show no significant periodicity above ~50% confidence. This 'yearly' model predicts a more damped response to temporal variations of seasonal stress changes. We statistically quantify the capacity of the models to constrain annual seasonal variations though the errors of the Schuster walks at 1 year period on synthetic catalogs (aleatoric uncertainty) with seasonal stress input to the observed walk (Figure 4F, Figure S7). Remarkably, the 1000 best models (accounting for epistemic uncertainty) using yearly TRS models show ~one order of magnitude larger errors in phase and amplitude of seasonality compared to the monthly TRS ones (Figure 4F). Using this seasonal analysis and the metrics to quantify seasonality, we can further tighten the constraints on the range of admissible parameters (Figure 4E, Figure S3B light blue dots). Finally, we evaluate the seasonality predicted by the instantaneous nucleation CF model in Figure 4E (yellow curves). This model strongly over-predicts seasonality and responds in phase to the maximum Coulomb stress rate, $\dot{\Delta S}$, (Ader & Avouac, 2013; Dempsey & Suckale, 2023), effectively showing that the nucleation process cannot be instantaneous.

Solid Earth tides -deformations of Earth's surface caused by gravitational forces- are another source of short-timescale stress variations that may also affect seismicity (Cochran, et al., 2004). In Groningen, the amplitude of stress variations due to tidal loads is <0.5 kPa (Figure S8, Supplementary Text) so ~40 times smaller than the estimated amplitude due to seasonal extraction variations, consistently with the observation that the Schuster spectrum doesn't reveal any detectable periodicity at the dominant semi-diurnal and diurnal tidal periods (Figure S6).

4 Conclusions and implications

Our results highlight the merit of accounting for the finite duration of earthquake nucleation and a possible initial strength excess to forecast induced seismicity. These two elements are needed to obtain a model that can predict the response of seismicity to stress changes on both short-and-long timescales, and we have proposed a method to quantify the goodness of fit to the short-timescales in addition to the conventional evaluation on long timescales. If the initial strength excess is ignored (Candela, et al., 2019), the seismicity response time can be overestimated by orders of magnitude leading to seismicity forecasts with a sustained seismicity tail because the delay between the start of operations and the onset of seismicity is adsorbed by a long characteristic nucleation time. This bias effectively shuts-down the effect of short-timescale stress variations, and over-predicts seismicity rates following decreases in fluid extraction rates (Figure 2B, (Heimisson, et al., 2022)). Alternative formulations than rate-and-state friction to account for a finite nucleation time should lead to a similar behavior (Dahm & Hainzl, 2022; Zhai, et al., 2019). This study shows that the seismicity response to seasonal stress variations at Groningen is consistent with the principle that stress variations result in an earthquake time advance (if the Coulomb stress change is positive) or delay (if the Coulomb stress change is negative) (Stein, 1999). This principle holds for earthquake nucleation models based on rate-and-state or coulomb friction with instantaneous failure. A Coulomb stress increase has the effect of bringing potential earthquake nucleation sites to failure but the transient increase in seismicity rate will drop as nucleation sites are consumed, and the duration of the transient is characterized by t_a^{acc}. The opposite occurs under a stress decrease. The total number of events averaged over a period of the order of t_a^{acc} or larger will not change if periodic stress variations are added over the mean stressing rate. Models with long (>1000yr) response times (Candela, et al., 2019) can give the impression that more events occur due to seasonal variations if the observation period is not long enough to capture the system's relaxation (Fig. 2b, and S4, green curves). Our study shows that t_a^{acc} is actually small enough (<10yr) that the seasonal variations of stress don't augment the seismicity averaged over an annual to multiannual time scale.

The mitigation of seismic hazard associated to subsurface fluid injection or extraction operations may be improved by accelerating model calibrations in three ways. First, the deployment of a sensitive seismic network well before starting subsurface operations, combined with enhanced earthquake detection techniques (Kong, et al., 2018) would help constrain the background seismicity rates (r, which presents a strong tradeoff with t_a, Figure S3) and reveal any induced seismicity early on, allowing for early calibration of the forecasting model. Second, varying fluid injection or production rates in a harmonic manner with various periods, would also help tighten the forecasting model (even if no correlated seismicity response is observed). Third, by performing shut-in operations over long enough time durations to track and constrain the relaxation of seismicity. Unbiased forecasting models of induced seismicity obtained by coupling pressure modelling with geomechanical deformation and seismicity should help mitigate the risk associated to the exploitation of subsurface reservoirs (geothermal, CO2 sequestration, hydrogen storage, hydrocarbon extraction).

Finally, stress variations at short-and-long times scales also affect natural systems (tectonic loading, post-seismic relaxation, hydrological/glacial load variations, and fault-to-fault interactions) and their seismicity response can provide insight into earthquake physics as shown here for induced seismicity. Commonly, in such studies, only one source of stress variations is considered, and our study shows that using a model calibrated at one time scale to forecast seismicity at another timescale can be flawed.

Acknowledgments

This study was supported by the NSF/IUCRC Geomechanics and Mitigation of Geohazards (National Science Foundation award # 1822214), and Extended Project GMG-3. M.A. Acknowledges funding from the Swiss National Science Foundation through grant P2ELP2_195127. We gratefully acknowledge data and support from Shell Global Solutions. Authors declare that they have no competing interests. We thank two anonymous reviewers for their helpful comments.

Open Research

The data needed to reproduce this article can be found in (Burkitov et al., 2016) and (Oates, et al., 2022). Codes necessary for the reproduction of figures in this article are available through (Acosta, et al., 2023).

References

Acosta, M. et al., 2023. Dataset and codes for : Earthquake nucleation characteristics revealed by seismicity response to seasonal stress variations induced by gas production at Groningen. [Software]. *Zenodo https://doi.org/10.5281/zenodo.8329298.*

Ader, T. J. & Avouac, J.-P., 2013. Detecting periodicities and declustering in earthquake catalogs using the Schuster spectrum, application to Himalayan seismicity. *Earth and Planetary Science Letters,* September, Volume 377-378, p. 97–105.

Ader, T. J., Lapusta, N., Avouac, J. P. & Ampuero, J. P., 2014. Response of rate-and-state seismogenic faults to harmonic shear-stress perturbations. *Geophysical Journal International,* Volume 198, p. 385–413.

Beeler, N. & Lockner, D., 2003. Why earthquakes correlate weakly with the solid Earth tides: Effects of periodic stress on the rate and probability of earthquake occurrence. *Journal of Geophysical Research,* Volume https://doi.org/10.1029/2001JB001518.

Bourne, S. J. & Oates, S. J., 2017. Development of statistical geomechanical models for forecasting seismicity induced by gas production from the Groningen field. *Geologie en Mijnbouw/Netherlands Journal of Geosciences,* Volume 96, p. s175–s182.

Bourne, S. J. & Oates, S. J., 2017. Extreme Threshold Failures Within a Heterogeneous Elastic Thin Sheet and the Spatial-Temporal Development of Induced Seismicity Within the Groningen Gas Field. *Journal of Geophysical Research: Solid Earth,* Volume 122, pp. 10,299–10,320.

Bourne, S. J. & Oates, S. J., 2020. Stress-Dependent Magnitudes of Induced Earthquakes in the Groningen Gas Field. *Journal of Geophysical Research: Solid Earth,* Volume 125.

Bourne, S. J., Oates, S. J. & van Elk, J., 2018. The exponential rise of induced seismicity with increasing stress levels in the Groningen gas field and its implications for controlling seismic risk. *Geophysical Journal International,* June, Volume 213, p. 1693–1700.

Bourne, S. J., Oates, S., van Elk, J. & Doornhof, D., 2014. A seismological model for earthquakes induced by fluid extraction from a subsurface reservoir. *Journal of Geophysical Research: Solid Earth,* Volume 119, p. 8991–9015.

Buijze, L. et al., 2017. Fault reactivation mechanisms and dynamic rupture modelling of depletion-induced seismic events in a Rotliegend gas reservoir. *Netherlands Journal of Geosciences,* December, Volume 96, p. s131–s148.

Burkitov et al., 2016. Groningen Field Review 2015 Subsurface Dynamic Modelling Report.. *Nederlandse Aardolie Maatschappij, https://nam-feitenencijfers.data-app.nl/download/rapport/e683753a-e085-417d-995d-b7ae7a9c820f?open=true.*

Candela, T. et al., 2019. Depletion-Induced Seismicity at the Groningen Gas Field: Coulomb Rate-and-State Models Including Differential Compaction Effect. *Journal of Geophysical Research: Solid Earth,* Volume 124, p. 7081–7104.

Candela, T. et al., 2022. Controls on the spatio-temporal patterns of induced seismicity in Groningen constrained by physics-based modelling with Ensemble-Smoother data assimilation. *Geophysical Journal International,* February, Volume 229, p. 1282–1308.

Candela, T., Wassing, B., ter Heege, J. & Buijze, L., 2018. How earthquakes are induced. *Science,* May, Volume 360, p. 598–600.

Chanard, K. et al., 2019. Sensitivity of Acoustic Emission Triggering to Small Pore Pressure Cycling Perturbations During Brittle Creep. *Geophysical Research Letters,* Volume 46, p. 7414–7423.

Cochran, E. S., Vidale, J. E. & Tanaka, S., 2004. Earth Tides Can Trigger Shallow Thrust Fault Earthquakes. *Science,* November, Volume 306, p. 1164–1166.

Dahm, T. & Hainzl, S., 2022. A Coulomb Stress Response Model for Time-Dependent Earthquake Forecasts. *Journal of Geophysical Research: Solid Earth,* September.Volume 127.

de Jager, J. & Visser, C., 2017. Geology of the Groningen field – an overview. *Netherlands Journal of Geosciences,* December, Volume 96, p. s3–s15.

de Waal, J. A., Muntendam-Bos, A. G. & Roest, J. P. A., 2015. Production induced subsidence and seismicity in the Groningen gas field – can it be managed?. *Proceedings of IAHS,* November, Volume 372, p. 129–139.

Dempsey, D. & Suckale, J., 2017. Physics-based forecasting of induced seismicity at Groningen gas field, the Netherlands. *Geophysical Research Letters,* Volume 44, p. 7773–7782.

Dempsey, D. & Suckale, J., 2023. Physics-Based Forecasting of Induced Seismicity at Groningen Gas Field, The Netherlands: Post Hoc Evaluation and Forecast Update. *Seismological Research Letters,* January, Volume 94, p. 1429–1446.

Dieterich, J., 1994. A constitutive law for rate of earthquake production and its application to earthquake clustering. *Journal of Geophysical Research,* Volume https://doi.org/10.1029/93JB02581.

Dost, B. & Kraaijpoel, D., 2013. The August 16, 2012 earthquake near Huizinge (Groningen). *KNMI reports.*

Dost, B., Ruigrok, E. & Spetzler, J., 2017. Development of seismicity and probabilistic hazard assessment for the Groningen gas field. *Netherlands Journal of Geosciences,* December, Volume 96, p. s235–s245.

Ellsworth, W. L., 2013. Injection-Induced Earthquakes. *Science,* Volume 341, p. 1225942–1225942.

Foreman-Mackey, D., Hogg, D. W., Lang, D. & Goodman, J., 2013. emcee: The MCMC Hammer. *Publications of the Astronomical Society of the Pacific,* February, Volume 125, p. 306.

Geertsma, J., 1973. Land Subsidence Above Compacting Oil and Gas Reservoirs. *Journal of Petroleum Technology,* June, Volume 25, p. 734–744.

Goebel, T. H. W. & Brodsky, E. E., 2018. The spatial footprint of injection wells in a global compilation of induced earthquake sequences. *Science,* August.

Grigoli, F. et al., 2017. Current challenges in monitoring, discrimination, and management of induced seismicity related to underground industrial activities: A European perspective. *Reviews of Geophysics,* Volume 55, p. 310–340.

Heimisson, E. R., Smith, J. D., Avouac, J.-P. & Bourne, S. J., 2022. Coulomb threshold rate-and-state model for fault reactivation: application to induced seismicity at Groningen. *Geophysical Journal International,* March, Volume 228, p. 2061–2072.

Heimisson, E. & Segall, P., 2018. Constitutive Law for Earthquake Production Based on Rate-and-State Friction: Dieterich 1994 Revisited. *Journal of Geophysical Research: Solid Earth,* Volume 123, p. 4141–4156.

Kühn, D. et al., 2022. A review of source models to further the understanding of the seismicity of the Groningen field. *Netherlands Journal of Geosciences,* Volume 101, p. e11.

Kaiser, J., 1950. Untersuchungen über das Auftreten von Geräuschen beim Zugversuch. *Dissertation Technische Hochschule München.*

Kaveh, H. et al., 2023. Induced Seismicity Forecasting with Uncertainty Quantification: Application to the Groningen Gas Field. *Authorea Preprints, doi:10.22541/au.168607320.06892091/v1.*

Kaven, J., Hickman, S., McGarr, A. & Ellsworth, W., 2015. Surface monitoring of microseismicity at the Decatur, Illinois, CO2 sequestration demonstration site.. *Seismological Research Letters,* Volume 86, p. 1096–1101.

King, G., Stein, R. & Lin, J., 1994. Static stress changes and the triggering of earthquakes. *Bulletin of the Seismological Society of America,* Volume 84, p. 935–953.

KNMI, 2023. KNMI Earthquake Catalog - Groningen - Last Accessed 2023.01.25.

Kong, Q. et al., 2018. Machine Learning in Seismology: Turning Data into Insights. *Seismological Research Letters,* November, Volume 90, p. 3–14.

Kuvshinov, B. N., 2008. Elastic and piezoelectric fields due to polyhedral inclusions. *International Journal of Solids and Structures,* March, Volume 45, p. 1352–1384.

Langenbruch, C., Weingarten, M. & Zoback, M. D., 2018. Physics-based forecasting of man-made earthquake hazards in Oklahoma and Kansas. *Nature Communications,* September, Volume 9, p. 3946.

Logg, A., Mardal, K.-A. & Wells, G., 2012. Automated Solution of Differential Equations by the Finite Element Method The FEniCS book.. *Lecture Notes in Computational Science and Engineering,* Volume Vol. 84..

Meyer, H., Smith, J. D., Bourne, S. J. & Avouac, J.-P., 2022. An integrated framework for surface deformation modeling and induced seismicity forecasting due to reservoir operations. *Geological Society, London, Special Publications,* August, Volume 528, p. SP528–2022–169.

Muntendam-Bos, A. G., 2020. Clustering characteristics of gas-extraction induced seismicity in the Groningen gas field. *Geophysical Journal International,* May, Volume 221, p. 879–892.

Muntendam-Bos, A. G. & De Waal, H., 2013. Reassessment of the probability of higher magnitude earthquakes in the Groningen gas field. *SODM reports,* January.

Muntendam-Bos, A. G. et al., 2022. An overview of induced seismicity in the Netherlands. *Netherlands Journal of Geosciences,* January, Volume 101, p. e1.

Muntendam-Bos, A. G., Roest, J. P. A. & Waal, H. A. d., 2017. The effect of imposed production measures on gas extraction induced seismic risk. *Netherlands Journal of Geosciences,* December, Volume 96, p. s271–s278.

Noël, C., Passelègue, F. X., Giorgetti, C. & Violay, M., 2019. Fault Reactivation During Fluid Pressure Oscillations: Transition From Stable to Unstable Slip. *Journal of Geophysical Research: Solid Earth,* Volume 124, p. 10940–10953.

Oates, S. et al., 2022. Geomechanical, seismological, and geodetic data pertaining to the Groningen gas field: a data package used in the "Mmax II Workshop", on constraining the maximum earthquake magnitude in the Groningen field. *Data Publication platform of Utrecht University, https://acc.epos-msl.uu.nl/dataset/b91f6311c0babb899e1aa5d9d79a2eb6,* September.

Post, R. A. J. et al., 2021. Interevent-time distribution and aftershock frequency in non-stationary induced seismicity. *Scientific Reports,* February, Volume 11, p. 3540.

Raleigh, C., Healy, J. & Bredehoeft, J., 1976. An experiment in earthquake control at Rangely, Colorado. *Science.*

Richter, G., Hainzl, S., Dahm, T. & Zöller, G., 2020. Stress-based, statistical modeling of the induced seismicity at the Groningen gas field, The Netherlands. *Environmental Earth Sciences,* May, Volume 79, p. 252.

Salvatier, J., Wiecki, T. V. & Fonnesbeck, C., 2016. Probabilistic programming in Python using PyMC3. *PeerJ Computer Science,* April, Volume 2, p. e55.

Scholz, C. H., 2019. The Mechanics of Earthquakes and Faulting.

Schuster, 1897. On lunar and solar periodicities of earthquakes |. *Proceedings of the Royal Society of London..*

Shirzaei, M. et al., 2016. Surface uplift and time-dependent seismic hazard due to fluid injection in eastern Texas. *Science,* September, Volume 353, p. 1416–1419.

Sijacic, D., Pijpers, F., Nepveu, M. & Thienen-Visser, K. v., 2017. Statistical evidence on the effect of production changes on induced seismicity. *Netherlands Journal of Geosciences,* December, Volume 96, p. s27–s38.

Smith, J. D. et al., 2019. Reconciling the Long-Term Relationship Between Reservoir Pore Pressure Depletion and Compaction in the Groningen Region. *Journal of Geophysical Research: Solid Earth,* Volume 124, p. 6165–6178.

Smith, J. D., Heimison, E. R., Bourne, S. J. & Avouac, J.-P., 2022. Stress-based forecasting of induced seismicity with instantaneous earthquake failure functions : Applications to the Groningen Gas Reservoir .. *Earth and Planetary Science Letters,* Volume 594.

Smith, J. D., White, R. S., Avouac, J. P. & Bourne, S. J., 2020. Probabilistic earthquake locations of induced seismicity in the Groningen region, the Netherlands. *Geophysical Journal International,* Volume 222, p. 507–516.

Stein, R. S., 1999. The role of stress transfer in earthquake occurrence.. *Nature,* 402(6762), pp. 605-609.

Trampert, J., Benzi, R. & Toschi, F., 2022. Implications of the statistics of seismicity recorded within the Groningen gas field. *Netherlands Journal of Geosciences,* Volume 101, p. e9.

van Thienen-Visser, K. & Breunese, J., 2015. Induced seismicity of the Groningen gas field: History and recent developments. *The Leading Edge,* Volume 34, p. 664–671.

Van Wees, J.-D.et al., 2017. Geomechanical models for induced seismicity in the Netherlands: inferences from simplified analytical, finite element and rupture model approaches. *Netherlands Journal of Geosciences,* December, Volume 96, p. s183–s202.

Walsh, F. & Zoback, M., 2015. Oklahoma's recent earthquakes and saltwater disposal. *Science Advances,* Volume 1.

Willacy, C. et al., 2018. Application of full-waveform event location and moment-tensor inversion for Groningen induced seismicity. *The Leading Edge,* February, Volume 37, p. 92–99.

Zaliapin, I. & Ben-Zion, Y., 2013. Earthquake clusters in southern California I: Identification and stability: Identification of Earthquake Clusters.. *Journal of Geophysical Research: Solid Earth,* June, Volume 118, p. 2847–2864.

Zhai, G., Shirzaei, M., Manga, M. & Chen, X., 2019. Pore-pressure diffusion, enhanced by poroelastic stresses, controls induced seismicity in Oklahoma. *Proceedings of the National Academy of Sciences,* August, Volume 116, p. 16228–16233.

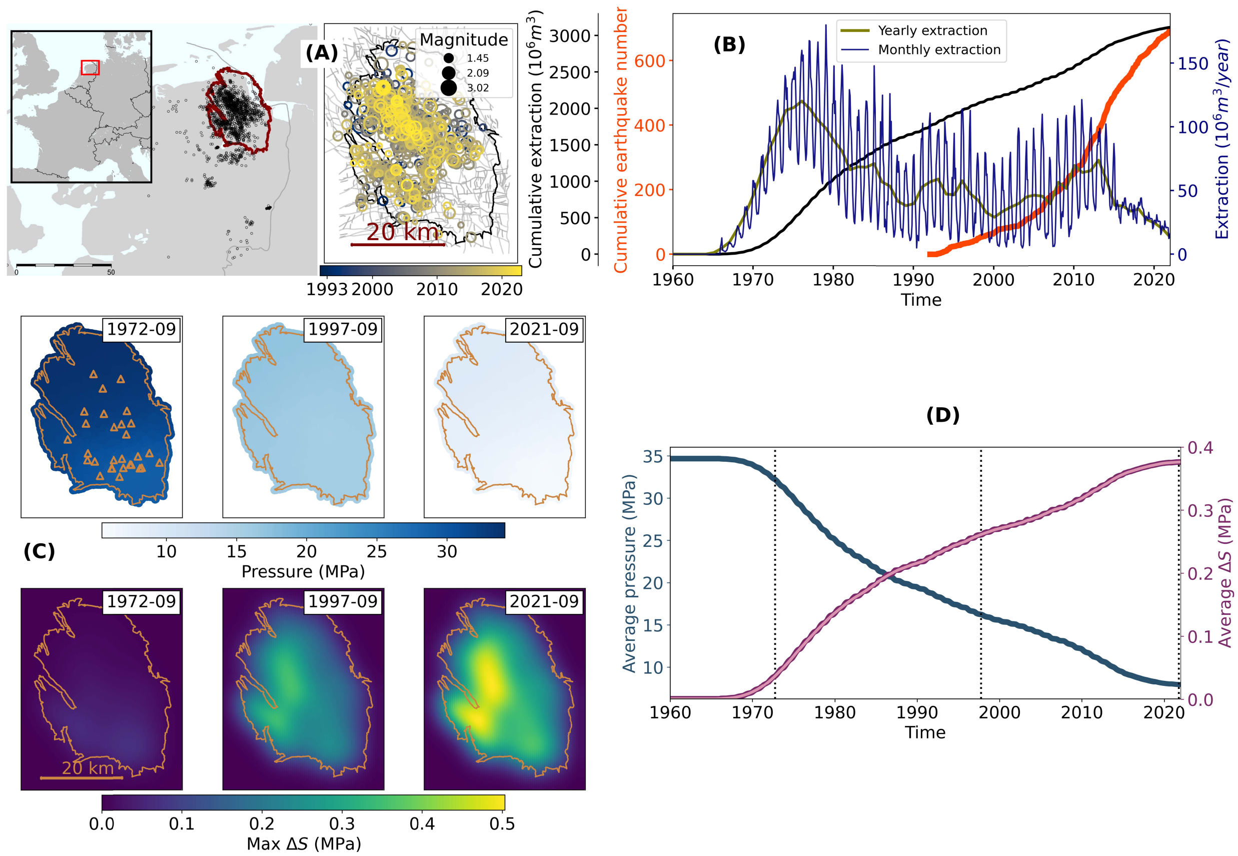

Figure 1. The Groningen gas field & simulation results.
(A) Geographic context showing extensive seismicity due to the gas field in an otherwise stable tectonic setting (left), and top view of the reservoir (right) showing identified faults (gray traces; (Oates, et al., 2022)), and the earthquake catalog (with magnitude ≥1.1; (Dost, et al., 2017; KNMI, 2023)) color coded by time. Sizes represent the earthquake magnitudes. **(B)** Observed data averaged over the gas reservoir versus time. Left y-axes shows cumulative extraction (black), and cumulative earthquake number (orange) since 1991, 34 years after the start of extraction. Right y-axis shows the discretized extraction data averaged either yearly (green line), or monthly (blue line). The monthly averaged extraction shows more than 80% seasonal variations with more gas extraction in the winter months. **(C)** Map view snapshots of simulation results at the dates shown in inset: fluid pressure (top row, with the position of extraction well clusters shown as triangles) and maximum Coulomb stress change calculated 10 m above the reservoir (ΔS, bottom row). **(D)** Simulation results averaged over the reservoir versus time. Left y-axis shows pressure (blue), and right y-axis shows maximum Coulomb stress changes (dark purple includes seasonal variations used as input for the monthly TRS model inversions, light purple shows smoothened seasonality used as input for the yearly TRS model inversions). Vertical dotted lines correspond to the snapshots shown in panel (C).

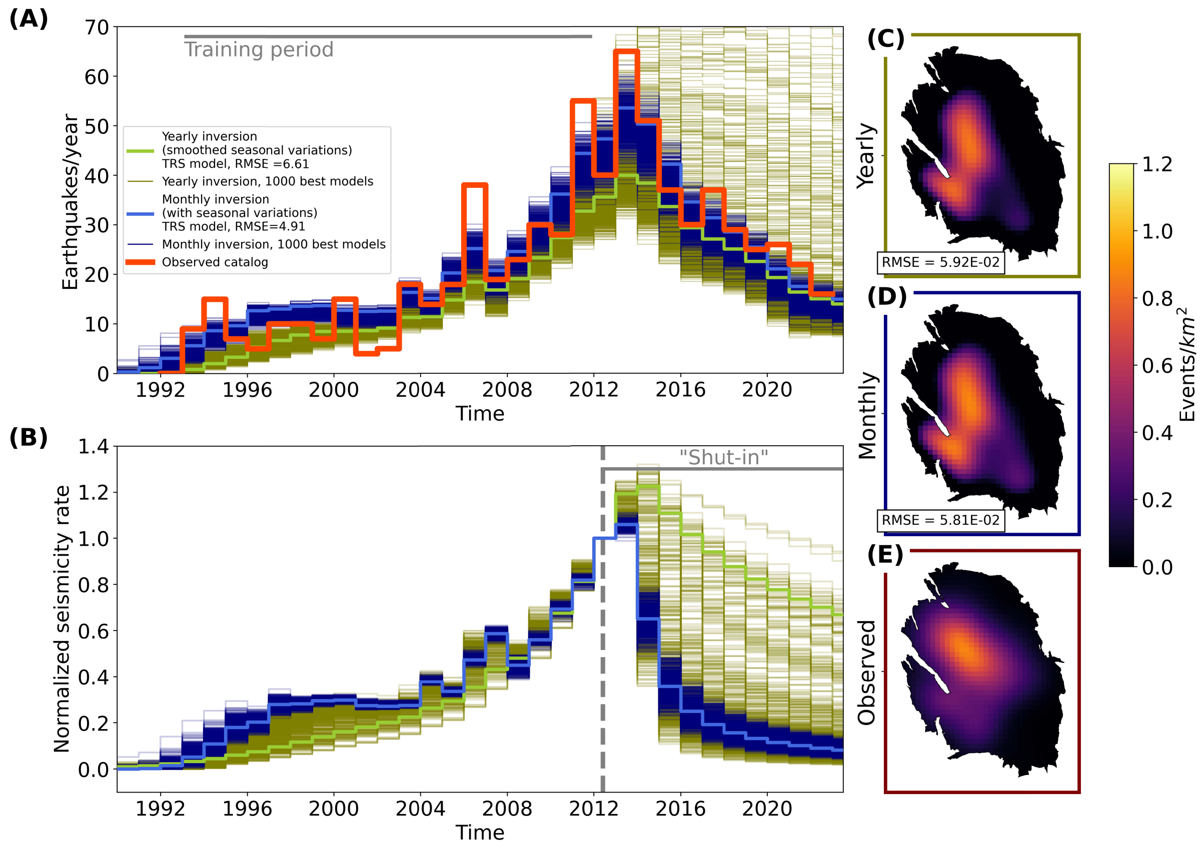

Figure 2. Yearly averaged seismicity rate forecasts for different models. (A) Earthquake rates comparing observed seismicity (orange curve, for $M \geq 1.1$), and inversions for the different models tested in this study. Green curves represent the yearly inversion (seasonality smoothened out in input Coulomb stress). Blue curves represent the monthly inversion (seasonality accounted for in input Coulomb stress). Thin lines represent the 1000 best models out of 50 000, accounting for epistemic uncertainty on model parameters. Thick lighter lines show the Maximum-A-Posteriori models from the MCMC inversion. Gray line represents the training period from 1993 to 2012. **(B)** Predicted seismicity rates for a hypothetical 'shut-in' of the reservoir with no change of Coulomb stress past 2012 (dashed gray line). All curves are normalized to 2012. A Coulomb failure model with instantaneous nucleation would predict an immediate drop of the seismicity to the background level. Colors correspond to the inversions in (A), and different lines represent the 1000 best models. **(C, D, E)** Epicentral event density for the MAP TRS models for yearly (C), monthly (D), and for the observed catalog (E).

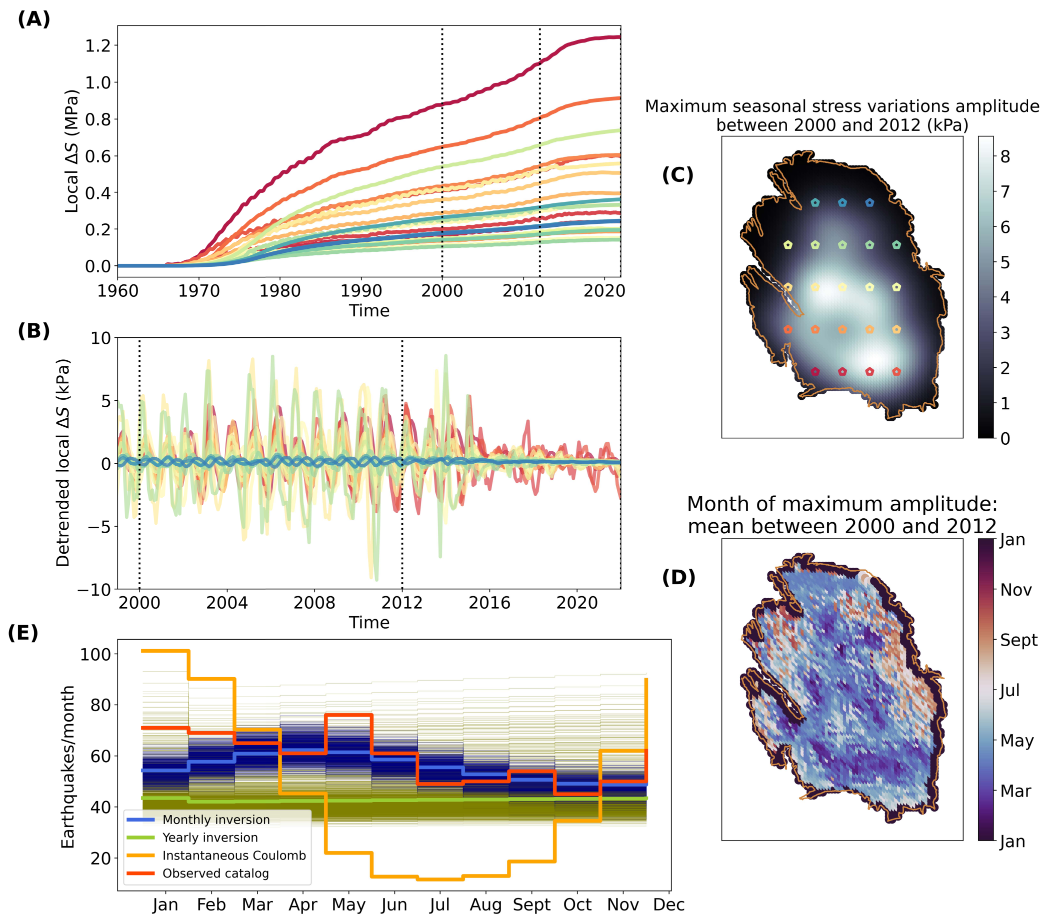

Figure 3. Spatial and temporal seasonal stress variations in the field & stacked seismicity. **(A)** Simulated local stress changes versus time at discrete locations color-coded in panel (C). **(B)** 12-month moving average detrended local stress changes at the same locations as in panel (A) versus time for the 1999-2021 period. The seasonal amplitudes of extraction and thus of stress changes were drastically reduced following the 2012 M_w3.6 Huizinge earthquake. **(C)** Map view of maximum seasonal stress variations peak-to-peak amplitude between 2000 and 2012. The points color-code locations at which local Coulomb stress evolution in time is shown in panels (A) and (B). **(D)** Mean month (during the 2000 to 2012 period) where the local maximum seasonal stress variations occur in the reservoir. The edges of the reservoir show a clear phase change for occurrence of maximum seasonal stress variations but have small amplitudes whereas the central and southern regions of the reservoir have in-phase large seasonal stress amplitudes (e.g., panel C). **(E)** Seasonal variation of seismicity rate obtained by stacking all years in the observed catalog (orange curve) compared with prediction of a Coulomb failure model with instantaneous nucleation (yellow curve, seismicity rate proportional to stress rate), and the stack of earthquake rates in our model inversions (accounting for epistemic uncertainty: green curves for the "yearly" models, blue for the "monthly" models).

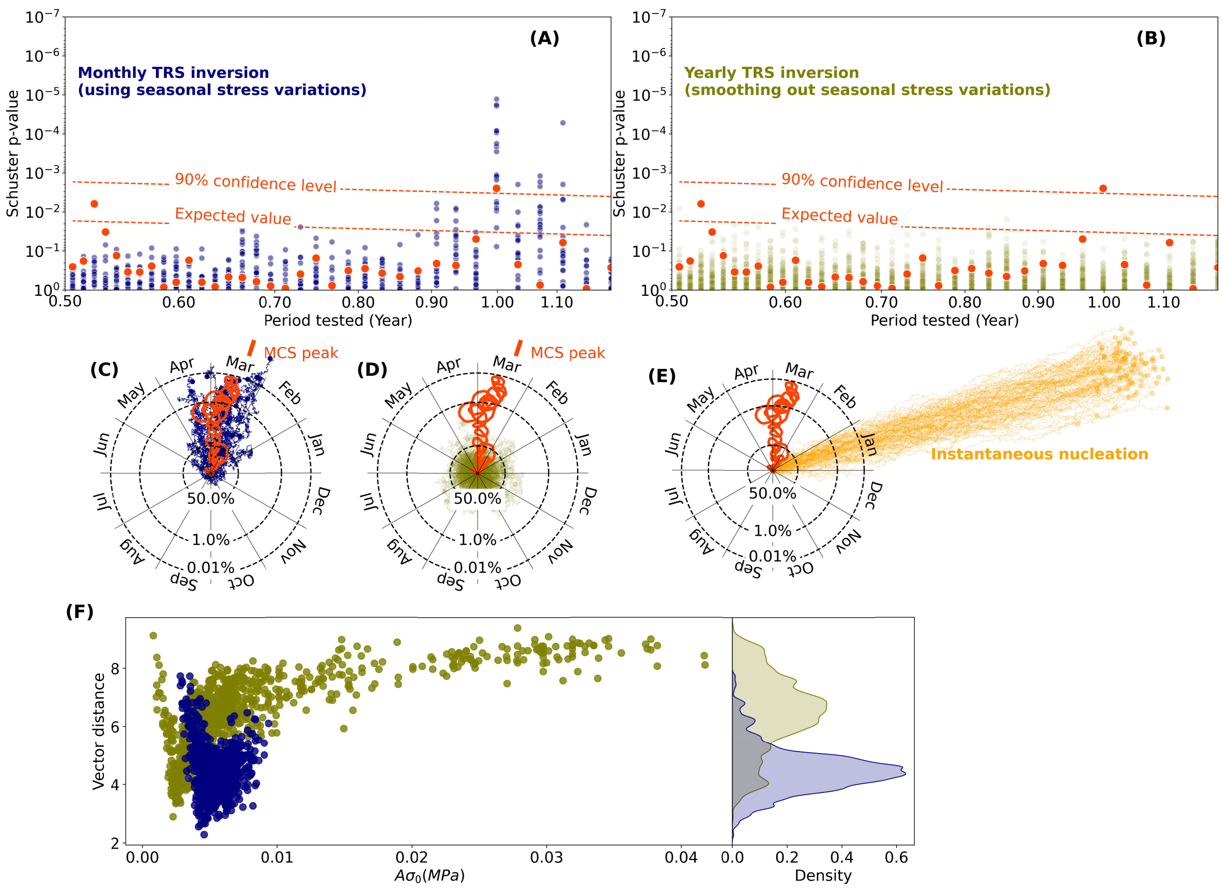

Figure 4. Quantitative constraints on earthquake nucleation models using seasonality. (A, B) Schuster spectrum (Ader & Avouac, 2013) for the observed catalog (with $M \geq 1.1$, orange points), and 100 synthetic catalogs (accounting for aleatoric uncertainty, Supplementary Material, Figure S5) derived from the yearly ((A), green points), and monthly ((B), blue points) MAP TRS models respectively. The Schuster spectrum is evaluated for periods from 6 to 18 months (a larger range of period spectra is shown in Figure S6). Low, isolated p-values quantify seasonality at a given period. **(C, D, E)** Schuster walks at 1 year period on the same catalogs as (A) and (B) respectively, and the instantaneous CF model (**(E),** orange lines). Circles denote the probability that the seismicity results from a random process at 50, 1, and 0.1% confidence levels. Drift direction reflects the times of year with the maximum seismicity rate. The orange tick mark (MCS) shows the phase of the maximum seasonal Coulomb stress averaged over the whole reservoir history (March-April). The observed catalog (orange lines) shows a clear maximum in seismicity rate toward March-April. This phase (and amplitude) is quantitatively recovered by the shown monthly TRS model (considering seasonal stress variations in input). The example yearly TRS model does not show signs of seasonality. The instantaneous CF model overestimates the seasonality. **(F)** Median vector distance error of synthetic catalogs (accounting for both epistemic and aleatoric uncertainty) to the observed catalog versus the parameter $A\sigma_0$ (Supplementary Material). The right-hand inset shows the error density

Figure 1.

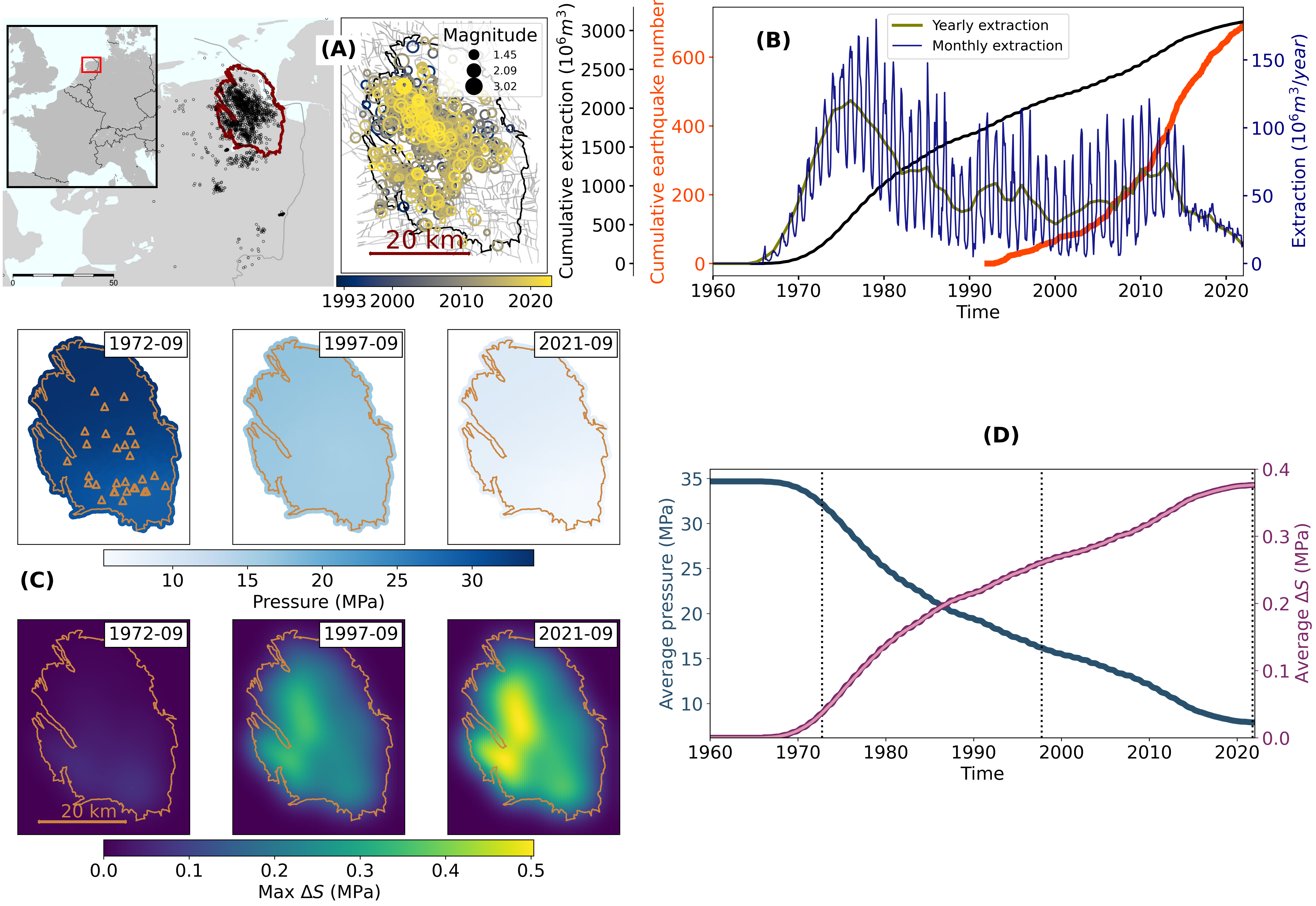

(A)
Magnitude
1.45
2.09
3.02
20 km
1993
2000
2010
2020
0
50
(B)
Yearly extraction
Monthly extraction
Cumulative extraction ($10^6 m^3$)
Cumulative earthquake number
Extraction ($10^6 m^3/year$)
Time
1972-09
1997-09
2021-09
(C)
Pressure (MPa)
Max ΔS (MPa)
20 km
(D)
Average pressure (MPa)
Average ΔS (MPa)
Time

Figure 2.

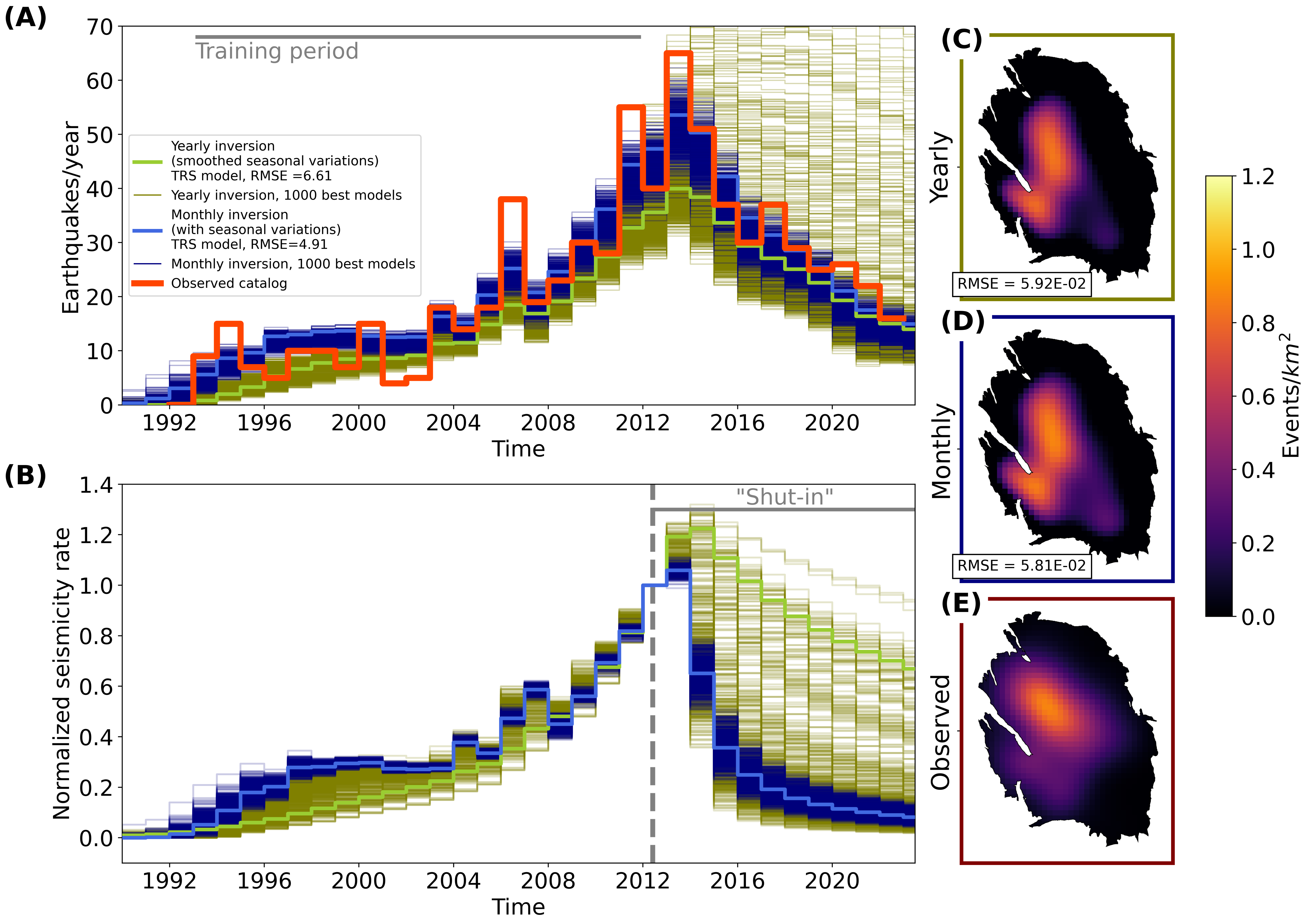
(A)
Training period
Earthquakes/year
Yearly inversion
(smoothed seasonal variations)
TRS model, RMSE =6.61
Yearly inversion, 1000 best models
Monthly inversion
(with seasonal variations)
TRS model, RMSE=4.91
Monthly inversion, 1000 best models
Observed catalog
Time
(B)
"Shut-in"
Normalized seismicity rate
Time
(C)
Yearly
RMSE = 5.92E-02
(D)
Monthly
RMSE = 5.81E-02
(E)
Observed
Events/km^2

Figure 3.

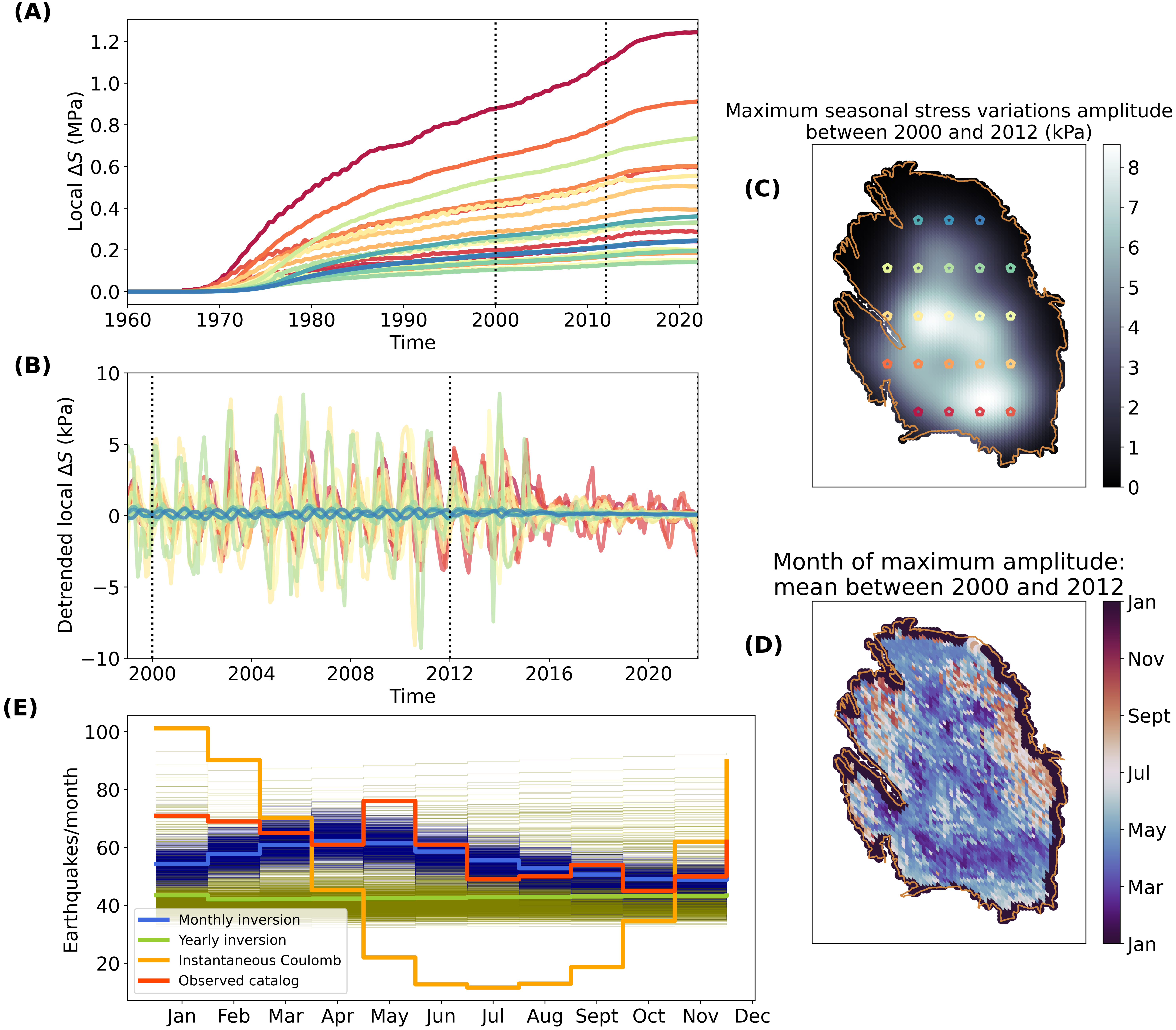

(A)
Local ΔS (MPa)
Time
(B)
Detrended local ΔS (kPa)
Time
(C)
Maximum seasonal stress variations amplitude
between 2000 and 2012 (kPa)
(D)
Month of maximum amplitude:
mean between 2000 and 2012
Jan
Nov
Sept
Jul
May
Mar
Jan
(E)
Earthquakes/month
Monthly inversion
Yearly inversion
Instantaneous Coulomb
Observed catalog
Jan
Feb
Mar
Apr
May
Jun
Jul
Aug
Sept
Oct
Nov
Dec

Figure 4.

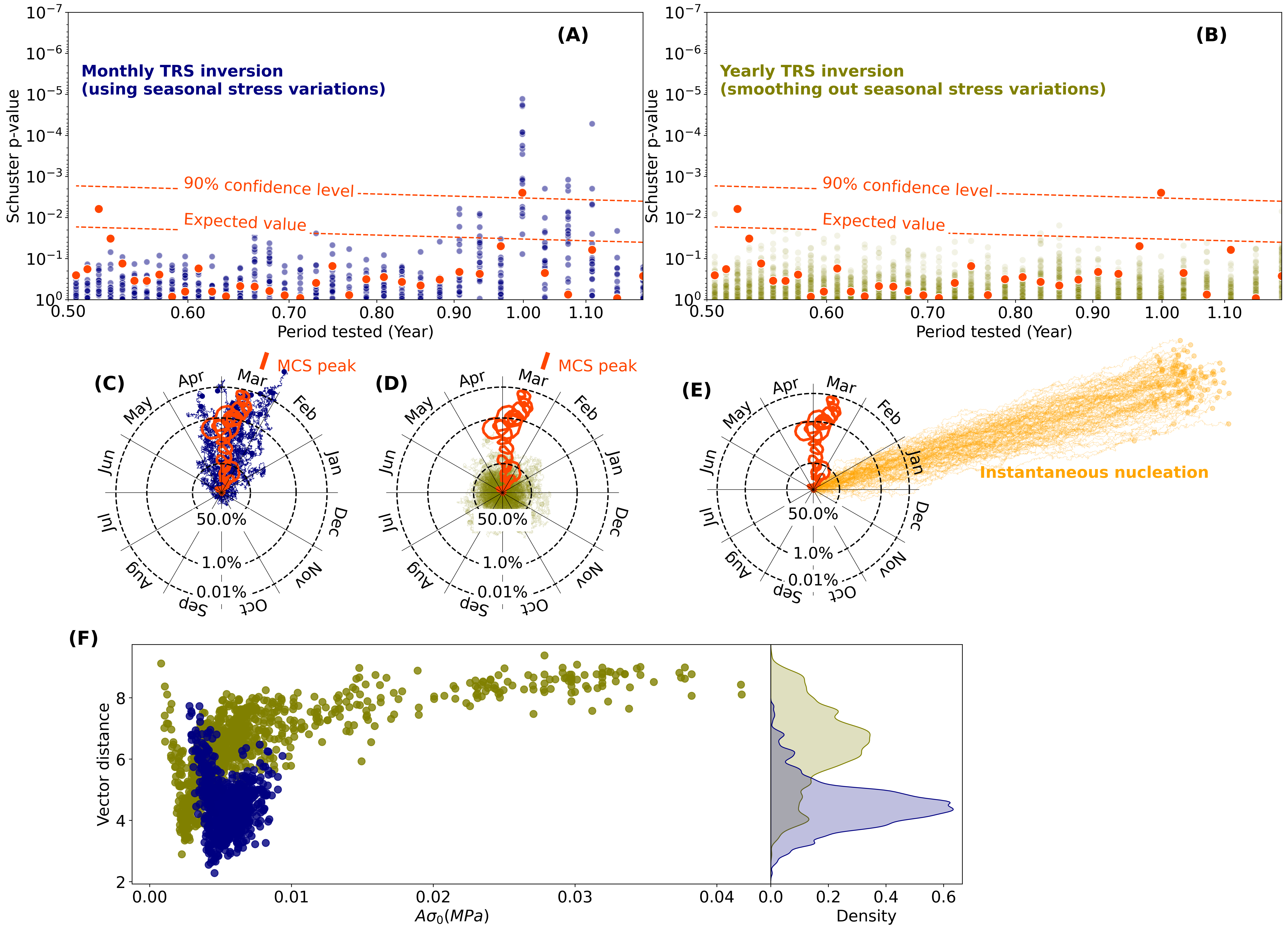

(A)
Monthly TRS inversion
(using seasonal stress variations)
90% confidence level
Expected value
Schuster p-value
Period tested (Year)
(B)
Yearly TRS inversion
(smoothing out seasonal stress variations)
90% confidence level
Expected value
Schuster p-value
Period tested (Year)
(C)
MCS peak
(D)
MCS peak
(E)
Instantaneous nucleation
Jan Feb Mar Apr May Jun Jul Aug Sep Oct Nov Dec
50.0%
1.0%
0.01%
(F)
Vector distance
$A\sigma_0(MPa)$
Density